ChemPubSoc Europe

DOI: 10.1002/cctc.201700916

CHEMCATCHEM Full Papers

# On the Role of Acidity in Bulk and Nanosheet [T]MFI (T = $Al^{3+}$, $Ga^{3+}$, $Fe^{3+}$, $B^{3+}$) Zeolites in the Methanol-to-Hydrocarbons Reaction

Lingqian Meng,[a] Xiaochun Zhu,[a, c] Brahim Mezari,[a] Robert Pestman,[a] Wannaruedee Wannapakdee,[a, b] and Emiel J. M. Hensen*[a]

The influence of framework substituents ($Al^{3+}$, $Ga^{3+}$, $Fe^{3+}$ and $B^{3+}$) and morphology (bulk vs. nanometer-sized sheets) of MFI zeolites on the acidity and catalytic performance in the methanol-to-hydrocarbons (MTH) reaction was investigated. The Brønsted acid density and strength decreased in the order Al(OH)Si > Ga(OH)Si > Fe(OH)Si ≫ B(OH)Si. Pyridine $^{15}N$ NMR spectra confirmed the differences in the Brønsted and Lewis acid strengths but also provided evidence for site heterogeneity in the Brønsted acid sites. Owing to the lower efficiency with which tervalent ions can be inserted into the zeolite framework, sheet-like zeolites exhibited lower acidity than bulk zeolites. The sheet-like Al-containing MFI zeolite exhibited the greatest longevity as a MTH catalyst, outperforming its bulk [Al]MFI counterpart. Although the lower acidity of bulk [Ga]MFI led to a better catalytic performance than bulk [Al]MFI, the sheet-like [Ga]MFI sample was found to be nearly inactive owing to lower and heterogeneous Brønsted acidity. All Fe- and B-substituted zeolite samples displayed very low catalytic performance owing to their weak acidity. Based on the product distribution, the MTH reaction was found to be dominated by the olefins-based catalytic cycle. The small contribution of the aromatics-based catalytic cycle was larger for bulk zeolite than for sheet-like zeolite, indicating that shorter residence time of aromatics can explain the lower tendency toward coking and enhanced catalyst longevity.

## Introduction

The realization that the glut of oil is not permanent has led to novel chemical conversion technologies to obtain chemicals and fuels from other feedstocks. Converting synthesis gas into liquid hydrocarbons can be achieved in two different manners. The Fischer–Tropsch process converts mixtures of CO and $H_2$ into long-chain paraffins. Introduced before the second world war in Germany, it has been further developed into commercial technology by SASOL and Shell.[1] The other route involves conversion of synthesis gas to methanol, a well-established process, prior to methanol dehydration to gasoline-range hydrocarbons in the Mobil process (methanol-to-gasoline, MTG).[2] Key to its initial commercialization was the discovery of a new zeolite, H-ZSM-5 (MFI topology),[3] allowing for a more narrow distribution of hydrocarbons than obtained with the Fischer–Tropsch synthesis process at high conversion. Overall, gasoline yields of 75–80 wt% can be realized in this manner.[2a] Although the decline in crude oil prices led to the discontinuation of the only running MTG plant in New Zealand, similar technologies to convert methanol to light olefins, primarily used as building blocks for polymers, have recently been commercialized, mainly in China.[4] For the conversion of methanol to olefins (MTO), small-pore zeolites are most effective, with silicoaluminophosphate H-SAPO-34 the commercially preferred catalyst.[5] This relatively weakly acidic catalyst allows light olefins to be obtained in yields higher than 80%.[5c,6] A major challenge is catalyst deactivation owing to the build-up of bulky aromatics in the cages of the chabazite structure.[2c,6a,7] These species cannot escape through the eight-membered ring (8MR) pore apertures of these small-pore zeolites.[8] Compared with H-SAPO-34, H-ZSM-5 used in the MTG process is less prone to deactivation, which is likely because aromatic

[a] L. Meng, X. Zhu, B. Mezari, R. Pestman, W. Wannapakdee, Prof. E. J. M. Hensen
Inorganic Materials Chemistry, Schuit Institute of Catalysis
Department of Chemical Engineering and Chemistry
Eindhoven University of Technology
5600 MB, Eindhoven (The Netherlands)
E-mail: e.j.m.hensen@tue.nl

[b] W. Wannapakdee
Department of Chemical and Biomolecular Engineering
School of Energy Science and Engineering
Vidyasirimedhi Institution of Science and Technology
Rayong 21210 (Thailand)

[c] X. Zhu
Current address:
State Key Laboratory of Heavy Oil Processing
The Key Laboratory of Catalysis of CNPC
College of Chemical Engineering
China University of Petroleum
Beijing 102249 (P. R. China)

The ORCID identification number(s) for the author(s) of this article can be found under: https://doi.org/10.1002/cctc.201700916.

products can leave the micropores through its 10MR pore system.[2d,5a] Although H-ZSM-5 produces a wider range of products in the gasoline range than 8MR zeolites, it can also be tuned to obtain propylene in high yield in the methanol-to-propylene process (MTP).[4a,5a]

There has been a long-standing debate on the mechanism of methanol conversion in zeolites.[9] A breakthrough was the realization by Kolboe and co-workers that a "hydrocarbon pool" is acting as reaction intermediates in methanol conversion reactions in zeolites.[10] Currently, it is widely accepted that there are two types of hydrocarbon pools, resulting in different cycles that convert methanol to higher hydrocarbons.[11] When olefins are the dominant intermediates, mainly propylene and higher hydrocarbons are the products of olefin methylation and cracking reactions.[11b,c] These olefins can be further converted into higher olefins, aromatics, and paraffins through oligomerization, cracking, aromatization, and hydrogen transfer reactions. Ethylene is obtained in very small amounts because of the low stability of primary carbenium ions.[12] When polymethylated benzenes contribute to methanol conversion as reaction intermediates, the ethylene yield is usually much higher because the polymethylated benzenes can undergo a series of *gem*-methylation, deprotonation, side-chain methylation, and elimination reactions.[13] Ultimately, the zeolite micropores become plugged because of the formation of polycyclic aromatics, high molecular weight polymeric carbon, amorphous carbon, and so forth.[14] In 8MR zeolites, in which polymethylated benzenes[15] cannot escape the scene of catalysis, the ethylene yield is typically much higher and deactivation more pronounced in comparison to zeolites with larger micropores.[2d,4a]

Performance in terms of product distribution and deactivation depends not only on the zeolite topology but also on the acidity of the zeolites.[16] Focusing on H-ZSM-5, various approaches have been followed to modify its acidity, mainly to decrease coking deactivation and influence product selectivity. Previous studies showed that doping H-ZSM-5 with elements such as P,[17] Fe,[18] Ga,[19] or B[16b,20] improved the selectivity of light olefins and/or prolonged the lifetime of catalysts. Recently, Yarulina et al. found that after incorporation of $Ca^{2+}$ in H-ZSM-5, a total light-olefin selectivity as high as 90% was obtained in the methanol-to-hydrocarbons (MTH) reaction and the catalyst showed improved lifetime.[21] Synthesis of MFI zeolites by using framework substituents other than $Al^{3+}$ (H-ZSM-5) has also been investigated as a way to tune the acidity.[22] Klinowski and co-workers found that the selectivity of aromatics in the MTH reaction depends strongly on the gallium concentration in gallosilicate MFI-type zeolites;[22a] borosilicate MFI-type zeolite showed extremely low activity in converting methanol to higher hydrocarbons.[22b,c,23]

Deactivation as a result of coking can lead to underutilization of the micropore space of zeolites, mainly because of diffusional limitations.[16c,24] Heavy deposits formed close to the external surface can block the access of methanol to the internal parts of the zeolite crystals. A common way to improve catalytic performance is then to decrease the size of the microporous domains, for instance, by using smaller zeolite crystals[25] or to introduce additional intra- or intercrystalline porosity in zeolites.[26] The latter solution has been followed in a wide variety of approaches, and methanol conversion has been a stock reaction in demonstrating the improved performance in terms of a decreased rate of deactivation, most evidently from the increased amount of methanol converted before the zeolite micropores become blocked. Examples of the latter include steaming,[27] desilication,[16c,28] and hard[29] and soft templating[24,30] methods to introduce additional porosity. An extreme case of control of hierarchical organization of micro- and mesopores was demonstrated by the group of Ryoo, who showed that diquaternary ammonium surfactants allow sheet-like zeolites to be obtained in which the crystal size is limited to several nanometers in one direction, the sheets are separated by mesopores.[30] Such zeolite samples display greatly improved catalytic performance in the MTH reaction.[16a,24]

In the present work, we set out to systematically investigate the role of acid strength in zeolite MFI by using Al, Ga, Fe, and B as framework substituents. Based on the literature,[31] it is expected that the acidity decreases in the order Al > Ga > Fe > B. As it has been shown that the presence of mesopores improves the utilization degree, we prepared both bulk MFI zeolites and sheet-like MFI zeolites by using the approach of Ryoo et al.[30] The obtained zeolites were extensively characterized for their morphological, textural, and acidic properties by elemental analysis, transmission electron microscopy (TEM), scanning electron microscopy (SEM), X-ray diffraction (XRD), Ar porosimetry, Fourier transform infrared (FTIR) spectroscopy, and solid-state NMR spectroscopy. We specifically focused on the extent of incorporation of the tervalent cations in the zeolite framework and the acid strength. The influence of acid strength and crystal domain size on the catalytic performance in the MTH reaction (activity, lifetime, amount of methanol converted, product distribution) will be discussed.

## Results and Discussion

### Structure and morphology

The XRD patterns of the bulk and sheet-like MFI zeolites are depicted in Figure 1. All patterns showed diffraction peaks characteristic for MFI zeolite,[16a] in which the relative intensity ratios of the dominant (011), (200), (031), and (051) reflections are practically similar. For all T substituents considered here, zeolites with the MFI topology were obtained. Different from bulk zeolites, only the *h*0*l* reflections in the XRD patterns of sheet-like MFI zeolites were sufficiently sharp for indexing. Corresponding to their small crystal size in the *b*-direction (i.e., the direction of the straight channels), the 0*k*0 reflections are strongly broadened or even absent.

Representative SEM and TEM images collected in Figure 2 indicate that all MFI zeolites synthesized by the structure directing agent (SDA) $C_{22\text{-}6\text{-}6}$•$Br_2$ exhibit a plate-like morphology. Although not uniform in thickness, the size of these nanosheets is on the order of several nanometers. There is no significant difference in morphology between the [Al]MFI, [Ga]MFI, [Fe]MFI, and [B]MFI nanosheet samples. The bulk zeolite con-

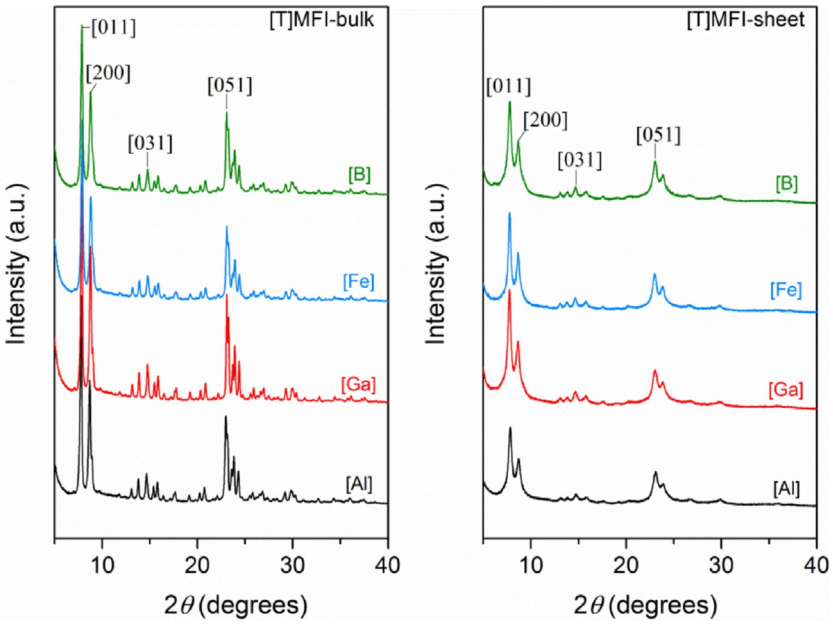


**Figure 1.** X-ray powder diffraction patterns of bulk and sheet-like MFI zeolites.

sists of large spherical particles with a size of several hundreds of nanometers as reported before.[32]

Figure 3 shows the Ar physisorption isotherms and corresponding pore size distributions (PSDs) of bulk and sheet-like MFI zeolites. All of the bulk MFI zeolites display the typical type I isotherms of microporous materials.[33] For the sheet-like zeolites, type IV isotherms with distinct hysteresis loops indicate the presence of mesopores next to micropores.[33,34] As the usual estimations for pore size distribution such as the Barrett–Joyner–Halenda (BJH) method are considered unreliable for the H4 type of isotherm,[33,34] we applied the NLDFT method using the adsorption branch of the isotherm. The PSDs demonstrate that the sheet-like zeolites contain a significant amount of mesopores in the 2–20 nm size range. The feature in the PSD around 2 nm is owing to the intersheet distance, whereas the broader feature can be ascribed to the voids between the stacks of sheets. The bulk MFI zeolites have few mesopores, which mainly originate from voids between the zeolite crystals. A distinct peak at 0.53 nm in the PSDs in all the zeolites corresponds to the size of the micropores of MFI zeolites.

**Table 1.** Textural properties of bulk and nanosheet MFI zeolites.

| Catalyst | $S_{BET}$[a] [$m^2 g^{-1}$] | $V_{total}$[b] [$cm^3 g^{-1}$] | $V_{meso}$[c] [$cm^3 g^{-1}$] | $V_{micro}$[d] [$cm^3 g^{-1}$] |
|---|---|---|---|---|
| [Al]MFI-bulk | 343 | 0.18 | 0.02 | 0.10 |
| [Ga]MFI-bulk | 435 | 0.22 | 0.03 | 0.13 |
| [Fe]MFI-bulk | 402 | 0.22 | 0.04 | 0.11 |
| [B]MFI-bulk | 353 | 0.18 | 0.03 | 0.10 |
| [Al]MFI-sheet | 567 | 0.81 | 0.68 | 0.13 |
| [Ga]MFI-sheet | 580 | 0.83 | 0.69 | 0.14 |
| [Fe]MFI-sheet | 511 | 0.77 | 0.63 | 0.13 |
| [B]MFI-sheet | 484 | 0.73 | 0.61 | 0.13 |

[a] Brunauer–Emmett–Teller (BET) surface area ($p/p_0 = 0.05–0.25$). [b] Total pore volume at $p/p_0 = 0.97$. [c] Mesopore volume by the NLDFT method using the adsorption branch. [d] The micropore volume of bulk MFI zeolite was determined by the *t*-plot method by using the Broekhoff–de Boer model (thickness range 0.34–0.50 nm); the micropore ($< 2.0$ nm) volume of sheet MFI zeolite was determined by the NLDFT method.

The textural properties derived from the Ar sorption isotherms are listed in Table 1. The texture does not change if the T atom is varied. All the sheet-like MFI zeolites have significantly higher Brunauer–Emmett–Teller (BET) surface area, total pore volume, and mesopore volume than their bulk counterparts. The BET surface area and the total pore volume of the sheet-like zeolites reached values as high as 580 $m^2 g^{-1}$ and 0.83 $cm^3 g^{-1}$, respectively. Mesopores contributed significantly to the total pore volume for these sheet-like zeolites. The micropore volume is comparable for bulk and sheet-like zeolites (typically in the 0.10–0.14 $cm^3 g^{-1}$ range).

The elemental composition of the samples is given in Table 3. The bulk and sheet-like [Al]MFI, [Ga]MFI, and [Fe]MFI zeolites have similar Si/T (T = Al, Ga, Fe) ratios ($\approx$45–50), indicating that nearly all substituent elements present in the synthesis gel were built into the zeolite framework. The Si/B atomic ratio was around 101 and 155 for bulk and sheet-like [B]MFI zeolites, respectively. This result is consistent with earlier findings that it is difficult introduce B into zeolite frameworks.[35] The primary cause for this is the small size of the boron cation in comparison to $Si^{4+}$.[35,36]

To investigate the location of Al, Ga, and B species in the calcined MFI zeolites, $^{27}Al$, $^{71}Ga$, and $^{11}B$ MAS NMR spectra were measured (Figure 4). The fraction of tetrahedral framework Al, Ga, and B species in zeolites are given in Table 2. For bulk and sheet-like [Al]MFI zeolites, the $^{27}Al$ MAS NMR spectra are dominated by a strong signal around 55 ppm corresponding to tetrahedrally coordinated framework Al ($Al^{IV}$).[24] A weaker signal around 0 ppm is related to extraframework Al species in octahedral coordination ($Al^{VI}$).[16a,24] The spectra do not contain the

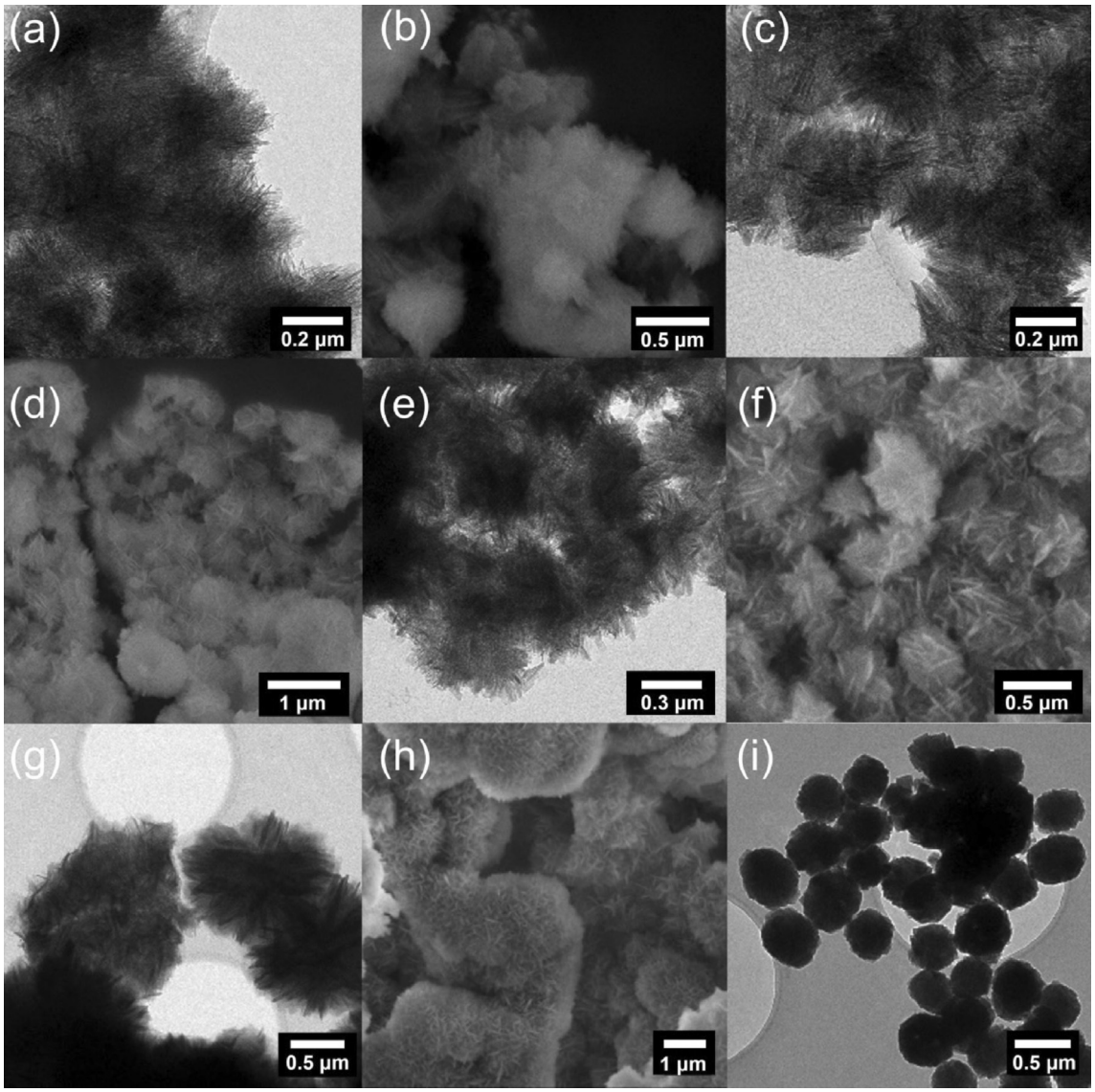


**Figure 2.** Representative SEM and TEM images of (a and b) [Al]MFI-sheet, (c and d) [Ga]MFI-sheet, (e and f) [Fe]MFI-sheet, (g and h) [B]MFI-sheet, and (i) [Al]MFI-bulk zeolites.

**Table 2.** Si/T ratio, fraction of framework T (T = Al, Ga, Fe, or B), and density of acid sites in the bulk and sheet-like MFI zeolites.

| Catalyst | T content[a] [wt%] | $Si/T_{total}$[a] | $T_{F,NMR}$[b] [%] | $Si/T_F$[c] | $T_{F,Si\,NMR}$[d] [%] | [BAS][e] [μmol $g^{-1}$] | [LAS][f] [μmol $g^{-1}$] |
|---|---|---|---|---|---|---|---|
| [Al]MFI-bulk | 0.98 | 45.0 | 95.1 | 52.3 | 86.0 | 265 | 75 |
| [Ga]MFI-bulk | 2.48 | 45.1 | n.d.[g] | 69.6 | 64.7 | 214 | 109 |
| [Fe]MFI-bulk | 1.98 | 45.7 | n.d. | n.d. | n.d. | 142 | 125 |
| [B]MFI-bulk | 0.18 | 101.4 | 98.3 | 125.4 | 80.5 | 42 | 33 |
| [Al]MFI-sheet | 0.93 | 47.2 | 83.6 | 60.7 | 77.4 | 211 | 122 |
| [Ga]MFI-sheet | 2.33 | 48.1 | n.d. | 109.0 | 44 | 125 | 210 |
| [Fe]MFI-sheet | 1.83 | 49.5 | n.d. | n.d. | n.d. | 153 | 140 |
| [B]MFI-sheet | 0.12 | 155.3 | 85.3 | 177.0 | 87.6 | 27 | 15 |

[a] Determined by ICP-OES analysis. [b] Determined by $^{27}Al$, $^{71}Ga$, and $^{11}B$ MAS NMR spectroscopy. [c] Fraction of framework T determined by $^{29}Si$ MAS NMR spectroscopy, spectra deconvoluted according to the strategy outlined by Fyfe et al., i.e., $Si/T_F = [Q_4(0T) + Q_4(1T) + Q_3(0T)]/Q_4(1T)$.[39] [d] Fraction of framework T determined by ICP-OES analysis and $^{29}Si$ MAS NMR spectroscopy, $T_{F,NMR}$ (%) = $(Si/T_{total})/(Si/T_F) \times 100$ %. [e] Density of Brønsted acid sites (BAS) determined by IR spectra of adsorbed pyridine after evacuation for 1 h at 423 K. [f] Density of Lewis acid sites (LAS) determined by IR spectra of adsorbed pyridine after evacuation for 1 h at 423 K. [g] Not determined.

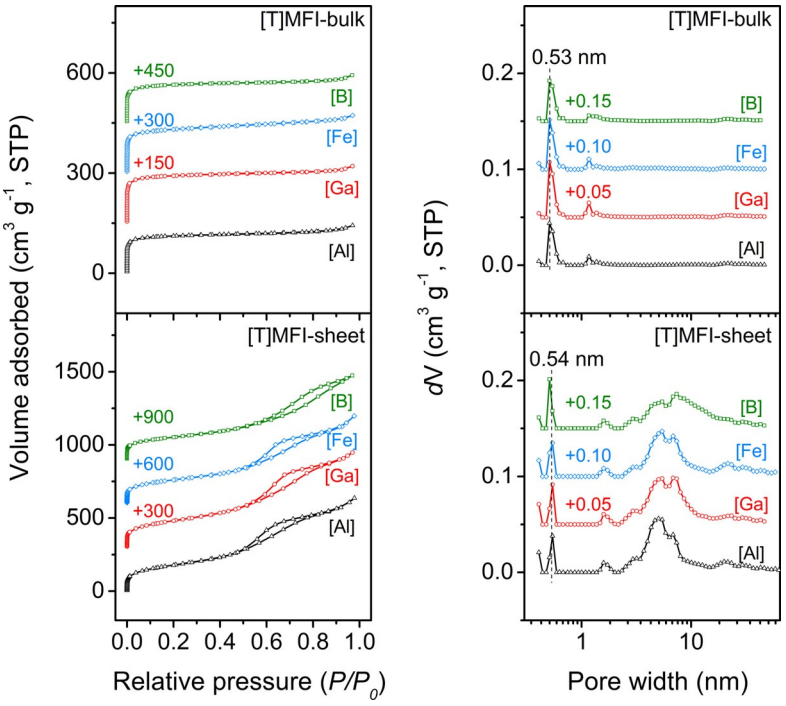


**Figure 3.** Ar physisorption isotherms (left) and pore size distribution (right) of bulk and sheet-like MFI zeolites. The pore size distributions were calculated by using the NLDFT method using the adsorption branch.

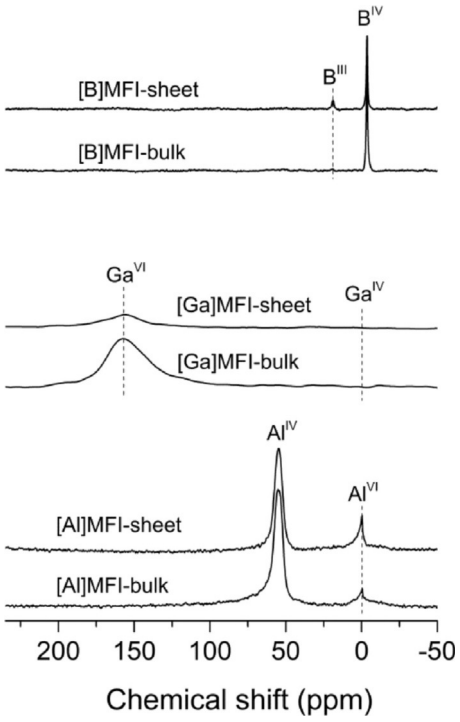


**Figure 4.** $^{27}$Al MAS NMR spectra of [Al]MFI-bulk and [Al]MFI-sheet, $^{71}$Ga MAS NMR spectra of [Ga]MFI-bulk and [Ga]MFI-sheet, $^{11}$B MAS NMR spectra of [B]MFI-bulk and [B]MFI-sheet.

feature around 30 ppm that is typical for five-coordinated Al and/or distorted tetrahedral Al species.[24] The fraction of $Al^{IV}$ in [Al]MFI-sheet of 84% is lower than that of 95% for [Al]MFI-bulk. This is in accord with earlier studies that reported the lower efficiency in building Al atoms into the MFI framework during nanosheet formation.[24]

For bulk and sheet-like [Ga]MFI zeolites, the $^{71}$Ga MAS NMR spectra contain a broad feature in the 100–200 ppm region, which is usually assigned to tetrahedrally coordinated framework Ga ($Ga^{IV}$) species.[22a,36b] The invisibility of the signal corresponding to octahedrally coordinated Ga ($Ga^{VI}$) has been ascribed to large electric field gradients over a fraction of the Ga nuclei and makes quantitative determination of the fraction of Ga inserted into the framework impossible.[36b]

The $^{11}$B MAS NMR spectra of bulk and sheet-like [B]MFI zeolites contain an intense feature at −3.6 ppm. This shows that most B atoms are present as tetrahedral species ($B^{IV}$) in the zeolite framework.[37] A weaker peak around 18–19 ppm corresponds to extraframework trigonal B species ($B^{III}$).[37a] There is no clear signal at 10 ppm, at which one expects trigonal framework B species in $B(OSi)_3$.[37a] It has been reported that exposure of the zeolites to a base such as $H_2O$ can convert the trigonal framework B species to tetrahedrally coordinated $B^{IV}$.[36a,37a,38] Similar with [Al]MFI, the [B]MFI-sheet zeolite contains a lower fraction of $B^{IV}$ species (85%) than its bulk counterpart (98%).

Figure 5 shows direct excitation (DE) $^{29}$Si NMR spectra of the [Al]MFI, [Ga]MFI, and [B]MFI zeolites. It has been demonstrated that the chemical shifts of Si species in different coordination modes in MFI zeolites do not depend on the substituent.[40] Accordingly, the $^{29}$Si NMR spectra of the samples were deconvoluted in a similar manner. A rather broad line centered at

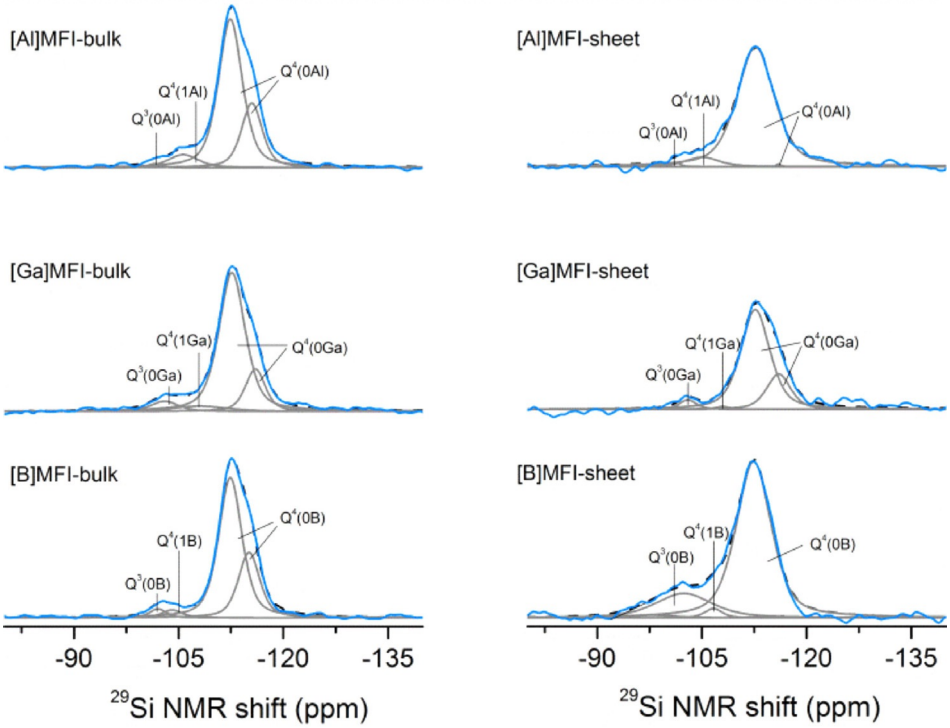


**Figure 5.** Direct-excitation $^{29}$Si MAS NMR spectra (blue solid line) of the zeolites. The grey lines indicate the deconvolution of the spectra, and the dashed lines show the integration of the grey lines.

−112 ppm is assigned to $Q^4 = Si(OSi)_4$ silicon atoms.[16a,24,40,41] In this range, two signals can be distinguished, a strong component at −112 ppm and a weaker one at −116 ppm, which are, respectively, assigned to symmetric and slightly asymmetric $Q^4$ silicon.[16a,39] The presence of tetrahedral Al, Ga, or B species in the zeolite framework is evident from the signal at −106 ppm in all of the spectra.[16a] The peak at −102 ppm corresponds to $Q^3 = Si(OSi)_3(OH)$ silicon atoms in zeolites.[24,39]

Table 2 lists the $Si/T_F$ (framework Al, Ga, or B) atomic ratios obtained by deconvolution of the $^{29}$Si MAS NMR spectra. By combining the framework substituent content with the value of $Si/T_{total}$ derived from elemental analysis, we obtain the fraction of T atoms in the zeolite framework as $T_{F,SiNMR}$ (%) = $(Si/T_{total})/(Si/T_F) \times 100\%$. Consistent with the $T_{F,NMR}$ determined by $^{27}$Al and $^{11}$B MAS NMR spectra, these data show that the largest part of the Al and B atoms were inserted into the framework. On the contrary, a significant fraction of the Ga atoms was located at extraframework positions in the [Ga]MFI zeolites. The relatively low fraction of Ga atoms inserted into the MFI zeolite framework is consistent with the findings of Choudhary et al.[42] Notably, the samples were calcined two times, once to remove the organic template and the second to remove ammonia after ion-exchange of the Na form. Release of water, predominantly in the first calcination step, results in steaming of the zeolites, a process that leads to the hydrolysis of Si-O-T bonds and the extraction of the substituents from the framework.[36b,42,43] The low framework site content of the calcined Ga-containing zeolites is consistent with the lower stability of tetrahedral Ga species in MFI zeolite in comparison to tetrahedral Al species.[36b] Others have studied the migration of Fe ions from the framework to extraframework positions in MFI zeolites.[44] A general conclusion is that the fraction of tetrahedral T atom substituents is lower in the sheet-like zeolites than in the corresponding bulk ones. This may be a result of the less rigid structure of the sheet-like zeolites, resulting in easier extraction during calcination[24] or the lower flexibility of the diquaternary structure-directing agent in comparison to TPA.

### Acidity characterization

The acid strength of the isomorphously substituted MFI zeolites was investigated by FTIR spectroscopy of adsorbed CO at 77 K of dehydrated samples (Figure 6). Before CO adsorption, all the zeolites show a characteristic OH stretching band around 3750 $cm^{-1}$, which can be assigned to terminal silanol groups.[31a,45] The concentration of these silanol groups is much higher in sheet-like zeolites than in bulk zeolites, which is owing to the higher external surface area. The weak band at 3740 $cm^{-1}$ present in some spectra is associated with internal isolated silanol groups.[45a,b] The band observed in the 3600–3650 $cm^{-1}$ region is assigned to T(OH)Si (bridging hydroxyl), the frequency of which depends on Brønsted acid strength.[31a] Consistent with the literature,[31a,45b,c] this band is located at 3616 $cm^{-1}$, 3626 $cm^{-1}$, 3634 $cm^{-1}$, and 3726 $cm^{-1}$ for Al[MFI], Ga[MFI], Fe[MFI], and B[MFI] zeolites, respectively, which is also consistent with acid strength decreasing in the order $Al(OH)Si > Ga(OH)Si > Fe(OH)Si \gg B(OH)Si$.[31a] The redshift of these bands following CO adsorption also depends on the

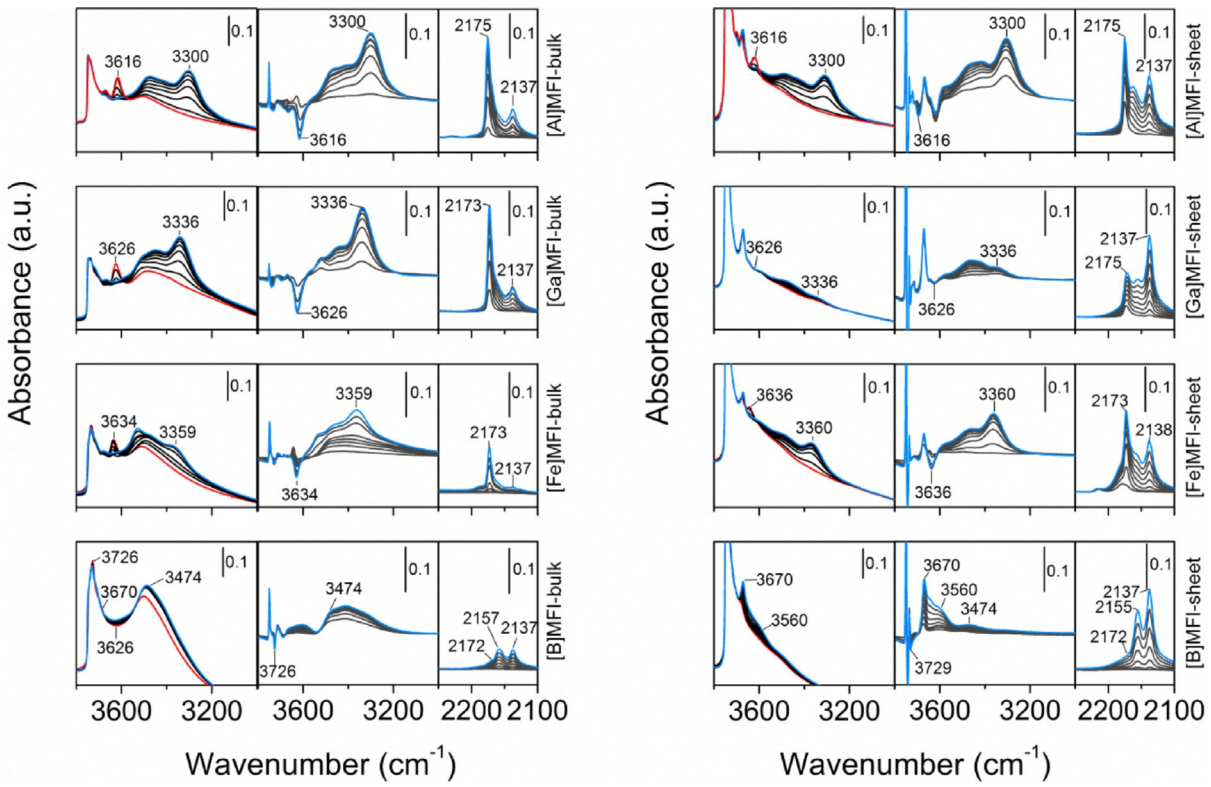


**Figure 6.** Hydroxyl (3800–3000 $cm^{-1}$) and carbonyl (2250–2100 $cm^{-1}$) stretching regions of FTIR spectra of dehydrated (left) bulk and (right) sheet-like MFI zeolites at 77 K as a function of the CO coverage before (hydroxyl and carbonyl stretch regions) and after (hydroxyl stretch region) subtraction of background spectra (difference spectra were normalized by weight). The red spectra represent the background spectra before CO adsorption in the OH stretching region.

acidity of bridging hydroxyls in the zeolites.[45c] For bulk and sheet-like [Al]MFI zeolites, the equal redshift of approximately 306 $cm^{-1}$ implies that the acid sites Al(OH)Si in these two forms of ZSM-5 zeolite have the same strength. If Al is replaced by Ga and Fe, the redshift decreases to approximately 290 $cm^{-1}$ and 275 $cm^{-1}$, respectively. Judging from the IR spectra, the amount of Brønsted acid sites in the two [B]MFI zeolites is very small and the corresponding redshift is the lowest among the MFI zeolites studied here. Moreover, the B-substituted zeolites appear to be highly defective with a large amount of silanol groups. The sheet-like zeolite is more defective than its bulk counterpart.

In the carbonyl stretching region, three bands at 2173 $cm^{-1}$, 2155 $cm^{-1}$, and 2138 $cm^{-1}$ can be observed, which belong to CO adsorption on Brønsted acidic sites, silanol groups, and physisorbed CO, respectively.[16a,24,46] The frequency of CO coordinating to the Brønsted acid sites does not depend on the type of substituent. Judging from the intensity of the band resulting from bridging hydroxyl groups, the number of acid sites decreases in the order Al(OH)Si ≈ Ga(OH)Si > Fe(OH)Si ≫ B(OH)Si. This order was as follows for the sheet-like zeolites: Al(OH)Si > Fe(OH)Si > Ga(OH)Si ≫ B(OH)Si.

Additional characterization of the acidity situation in these zeolites was obtained by low-temperature $^{1}H$-$^{15}N$ CPMAS NMR experiments (223 K) after adsorption of pyridine-$^{15}N$ (Figure 7). The NMR spectra of the zeolites showed three broad signals, which can be assigned based on the literature.[47] The signal in

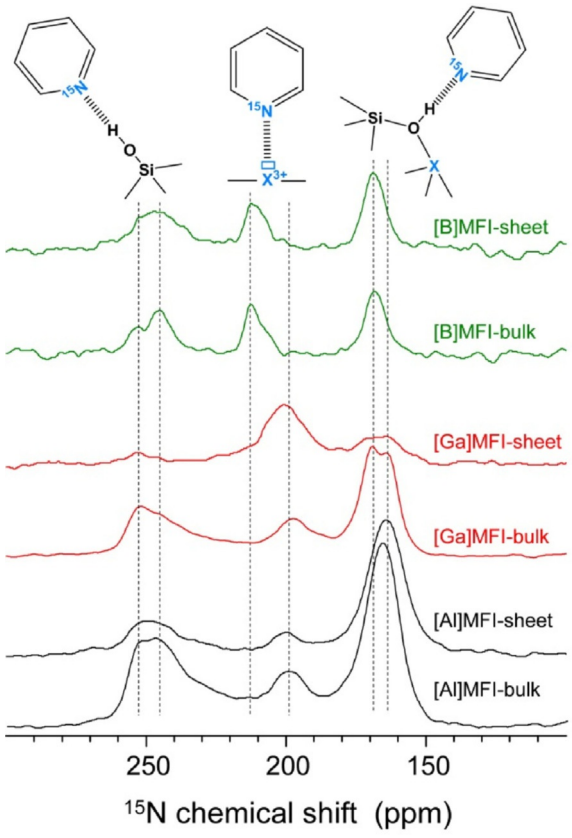


**Figure 7.** $^{1}H$-$^{15}N$ CPMAS NMR spectra of pyridine-$^{15}N$ absorbed on MFI zeolites. All the spectra were measured at 223 K.

the 140–185 ppm range relates to pyridinium ions formed by protonation of pyridine-$^{15}$N. Signals in the 185–220 ppm range correspond to interactions of the $^{15}$N lone pair with electron-deficient Lewis acid sites. Finally, signals in the 220–280 ppm range can be related to hydrogen bonding between pyridine-$^{15}$N with silanol groups.[47] It can be seen that the signal related to Brønsted acid sites appeared at higher magnetic field in [Al]MFI zeolites than in [B]MFI zeolites. This is consistent with the higher acid strength of the former zeolite. The bulk and sheet-like [Ga]MFI zeolites contain two distinct signals in the 140–185 ppm range, suggesting that there are two types of Brønsted acid sites. This might relate to the specific location of the isomorphous substitution in the MFI zeolite. Although most pronounced for [Ga]MFI, the spectra of Al(OH)Si and B(OH)Si also contain indications for the presence of two types of Brønsted acid sites.

Two signals at 253 ppm and 246 ppm observed in all of the spectra are related to hydrogen bonding between pyridine-$^{15}$N and external and internal silanol groups, respectively. The chemical shifts related to pyridine-$^{15}$N coordinating to Lewis acid sites are similar for [Al]MFI and [Ga]MFI zeolites. For [B]MFI zeolites, the signal occurs at lower magnetic field, characteristic of the weaker interaction between pyridine-$^{15}$N and Lewis acid B sites.

The density of Brønsted and Lewis acid sites was determined by use of IR spectroscopy of adsorbed pyridine. The spectra in the range 1580–1400 cm$^{-1}$ are shown in Figure 8. To quantify the total amount of Brønsted and Lewis acid sites, molar extinction coefficients of 0.73 cm μmol$^{-1}$ and 1.11 cm μmol$^{-1}$ were used, respectively.[48] These molar extinction coefficients were determined previously for the HZSM-5 zeolite,[48] and they are assumed to be independent of the zeolite topology and the strength of the acid sites.[49] The IR bands at 1545 cm$^{-1}$ and 1455 cm$^{-1}$ are assigned to pyridine associated with Brønsted and Lewis acid sites, respectively.[48] The band at 1490 cm$^{-1}$ arises from both types of pyridine.[50]

The corresponding densities of acid sites determined after evacuation at 423 K are listed in Table 2. Clearly, [Al]MFI-sheet zeolite contains less Brønsted acid sites than its bulk counterpart. The difference is much larger between [Ga]MFI-sheet and [Ga]MFI-bulk and is consistent with the lower fraction of tetrahedrally coordinated Al and Ga in sheet-like MFI zeolites as determined by NMR spectroscopy. Thus, the sheet-like zeolites contain more Lewis acid sites in the form of extraframework Al or Ga species than the bulk ones. The density of Brønsted and Lewis acid sites in bulk and sheet-like [Fe]MFI zeolites are comparable. Both bulk and sheet-like [B]MFI zeolites contain relatively small amounts of Brønsted and Lewis acid sites.

For bulk MFI zeolites, the density of Brønsted acid sites decreases in the order Al > Ga > Fe > B, which is consistent also with the CO IR data. Whilst no NMR data are available for Fe-containing zeolites, the pyridine IR spectra show that the

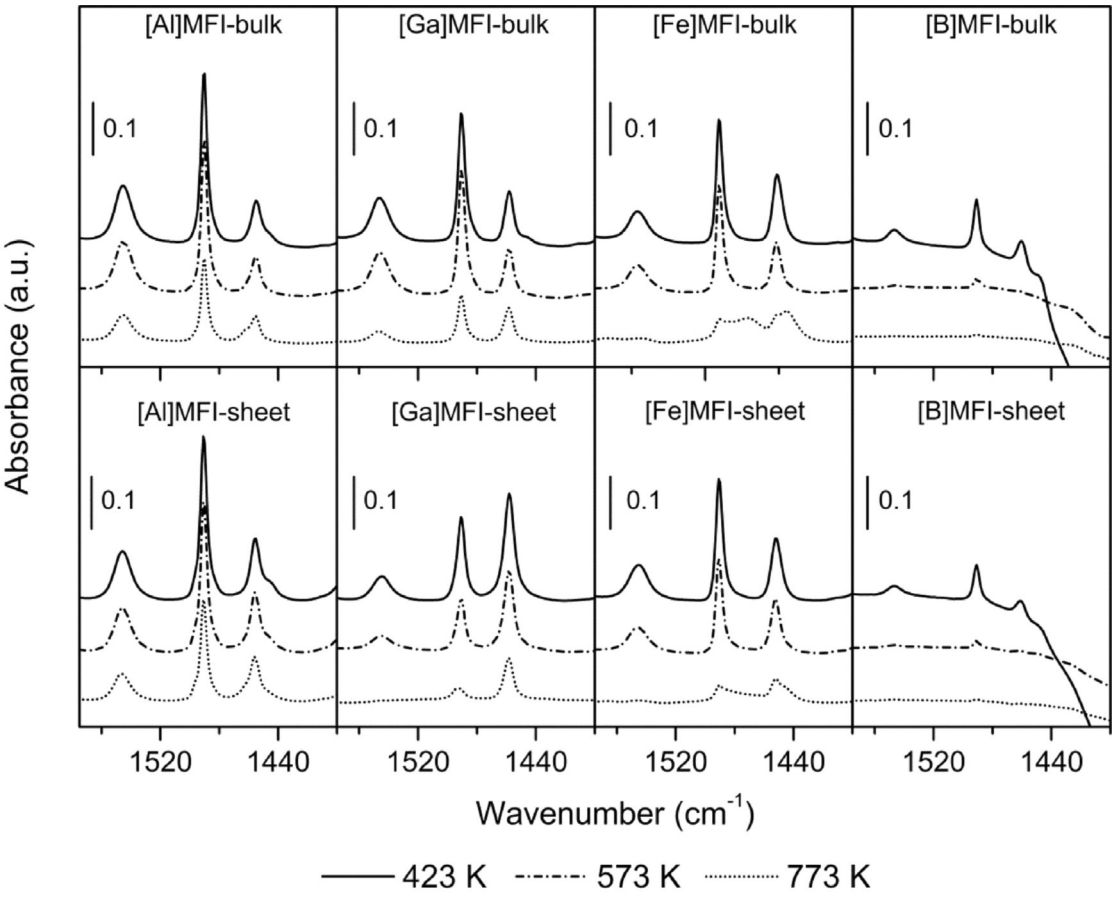


**Figure 8.** IR spectra of pyridine adsorbed on bulk and sheet-like MFI zeolites after evacuation at 423 K, 573 K, and 773 K.

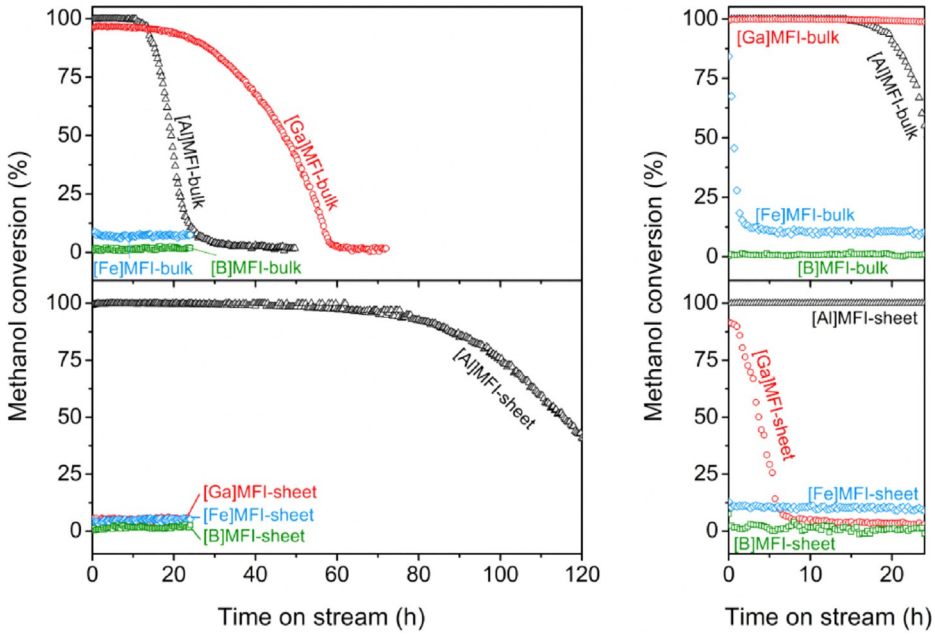


**Figure 9.** Catalytic performance of MFI zeolites in the methanol-to-hydrocarbons reaction (reaction conditions: WHSV = 6 $h^{-1}$ and 2 $h^{-1}$, $T$ = 673 K).

amount of Brønsted and Lewis acid sites in [Fe]MFI-bulk and [Fe]MFI-sheet zeolites are comparable. As the Brønsted acid site density is much lower in [Fe]MFI-bulk than in [Ga]MFI-bulk, we can estimate that the fraction of framework Fe ions is also much lower than the approximately 65% of Ga ions built into the [Ga]MFI-bulk framework. A similar analysis shows that the amount of Fe built into the sheet-like zeolite should be higher than the fraction of 44% of Ga ions built into [Ga]MFI-sheet. Taken together, this suggests that the fraction of Fe built into the framework is around 50–60%.

### Catalytic activity measurements

The results of methanol conversion as a function of time on stream obtained in a fixed-bed reactor at 673 K and two different space velocities (2 $h^{-1}$ and 6 $h^{-1}$) are presented in Figure 9. Dimethyl ether (DME) is considered as a reactant in the following discussion. The product selectivities of methane, ethane, ethylene, propane, propylene, $C_{4+}$ aliphatics and aromatics are collected in Table 3. Ethylene selectivity was used as an indicator for the degree of the propagation through polymethylated benzenes,[51] whereas the $C_{4+}$ selectivity was used for assessing the importance of propagation through the olefins-based cycle.[51]

We will discuss the activity results by comparing bulk and sheet-like zeolites. It is seen that [Al]MFI-sheet zeolite remains active much longer than its bulk counterpart at weight hourly space velocity (WHSV) values of 2 $h^{-1}$ and 6 $h^{-1}$. This result is in line with earlier studies, demonstrating the superior performance of the nanostructured zeolite.[16a,24] At a WHSV of 6 $h^{-1}$, the $C_{4+}$ selectivity for the sheet-like zeolite is 53%. The low ethylene (2.6%) in comparison to propylene (42.2%) selectivity points to the dominance of the olefins-based cycle in methanol conversion for the [Al]MFI-sheet zeolite.[16e] Owing to the short diffusion lengths in sheet-like MFI zeolites, the residence time of aromatics will be much shorter than in bulk MFI zeolites and the aromatics-based cycle, which produces ethylene, is suppressed. In contrast, [Al]MFI-bulk exhibits significantly higher ethylene (≈9%) and aromatics selectivities. The propylene selectivity is much higher than ethylene selectivity, indicating that an olefins-based cycle remains important. The higher coke content of the spent bulk zeolite sample is also consistent with this mechanistic difference, as we expect that heavy deposits are built up more rapidly in the aromatics-based cycle than in the olefins-based cycle.

Although [Ga]MFI-bulk was not able to convert all the methanol at the highest WHSV, it exhibited much higher stability in methanol conversion than [Al]MFI-bulk. We discuss two possible explanations. First, [Ga]MFI-bulk contains less Brønsted acid sites than [Al]MFI-bulk.[16a,46] Second, these acid sites are weaker in the gallosilicate than in the aluminosilicate. Both aspects may contribute to a lower rate of secondary reactions that result in the formation of more bulky products. Based on the selectivities, we infer that the aromatics-based cycle contributes less in the gallosilicate, possibly because of the high acidity required for aromatization of linear olefins. Surprisingly, the [Ga]MFI-sheet zeolite displayed very poor activity in methanol conversion. Besides the lower amount of Brønsted acid sites, a significant fraction of these sites also shows weak acidity in comparison to the sites in [Al]MFI, as followed from the pyridine-$^{15}$N NMR data. At higher WHSV, methanol conversion is low with $CH_4$, CO, and $CO_2$ contributing significantly to the products. A likely mechanism for such products is hydride transfer between methanol and surface methoxy species, with the resulting formaldehyde rapidly decomposing to CO.[52] Methanol conversion at low WHSV is initially approximately 90%. Under these conditions, the product distribution is similar to that of the other active zeolites with the olefins-based

**Table 3.** Lifetime, turnover number (TON), product distribution (after 25 min on stream), and coke content of MFI zeolite catalysts for the MTH reaction (WHSV = 6 $h^{-1}$ and 2 $h^{-1}$; $T$ = 673 K).

| Zeolite | WHSV [$h^{-1}$] | TON[a] | Selectivity [%] | | | | | | | Coke[c] [%] |
|---|---|---|---|---|---|---|---|---|---|---|
| | | | $C_1$[b] | $C_2^=$ | $C_2$ | $C_3^=$ | $C_3$ | $C_{4+}$ | Aromatics | |
| [Al]MFI-bulk | 6 | $1.3\times10^4$ | 0.4 | 9.1 | 0.1 | 29.5 | 4.1 | 49.3 | 7.5 | 10.1 |
| | 2 | – | 0.7 | 11.2 | 0.3 | 23.6 | 4.8 | 64.7 | 4.7 | – |
| [Ga]MFI-bulk | 6 | $3.6\times10^4$ | 0.3 | 3.0 | <0.1 | 38.6 | 1.5 | 54.9 | 1.6 | 5.3 |
| | 2 | – | 0.4 | 4.8 | <0.1 | 40.2 | 1.4 | 50.9 | 2.2 | – |
| [Fe]MFI-bulk | 6 | – | 66.5 | 3.3 | 0.4 | 13.3 | 1.0 | 12.7 | 2.8 | 6.9 |
| | 2 | $7.6\times10^2$ | 6.6 | 8.3 | 0.1 | 19.3 | <0.1 | 31.4 | 34.2 | – |
| [B]MFI-bulk | 6 | – | 100 | <0.1 | <0.1 | <0.1 | <0.1 | <0.1 | <0.1 | – |
| | 2 | – | 100 | <0.1 | <0.1 | <0.1 | <0.1 | <0.1 | <0.1 | – |
| [Al]MFI-sheet | 6 | $9.6\times10^4$ | 0.2 | 2.6 | <0.1 | 42.2 | <0.1 | 52.7 | 2.2 | 1.7 |
| | 2 | – | 1.3 | 6.9 | <0.1 | 32.7 | 2.1 | 52.0 | 5.0 | – |
| [Ga]MFI-sheet | 6 | – | 28.6 | 14.8 | 1.8 | 21.2 | 6.3 | 21.8 | 5.6 | 1.7 |
| | 2 | $2.0\times10^3$ | 0.8 | 2.0 | <0.1 | 35.0 | 0.6 | 48.8 | 12.8 | – |
| [Fe]MFI-sheet | 6 | – | 89.0 | 2.1 | <0.1 | 3.4 | <0.1 | 4.5 | <0.1 | 2.6 |
| | 2 | – | 62.0 | 2.0 | 1.8 | 2.2 | 2.6 | 4.8 | 24.6 | – |
| [B]MFI-sheet | 6 | – | 100 | <0.1 | <0.1 | <0.1 | <0.1 | <0.1 | <0.1 | – |
| | 2 | - | 100 | <0.1 | <0.1 | <0.1 | <0.1 | <0.1 | <0.1 | – |

[a] Turnover number of moles of methanol converted into products other than dimethyl ether before deactivation of catalyst per BAS; the concentration of BAS is the value from pyridine IR after evacuation at 423 K. [b] $CH_4$, CO, and $CO_2$. [c] Determined by TGA analysis after 24 h on stream.

cycle being dominant. With time on stream, however, an increase in aromatics selectivity was observed before deactivation, which may be attributed to the role of extraframework Ga species in the aromatization of olefins.[22a] [Fe]MFI-bulk shows much lower activity than [Ga]MFI-bulk and [Al]MFI-bulk, which is owing to the low acid strength. Despite the low conversion, the aromatics selectivity for the [Fe]MFI-bulk increased to 34% at the expense of propylene and $C_{4+}$ formation at low WHSV. At high WHSV, $CH_4$, CO, and $CO_2$ were the dominant products. The two [B]MFI zeolites display very low methanol conversion. Previously, it has been suggested that Al at the impurity level is responsible for the catalytic activity of B-containing zeolites.[23] Elemental analysis showed that both zeolites contain less than 10 ppm Al. Given this almost negligible amount, we attribute the residual activity of the two [B]MFI zeolites to a small amount of bridging OH sites. The products were mainly CO, $CO_2$, and $CH_4$.

To better investigate the influence of acid strength of MFI zeolites in the MTH reaction, we determined the turnover number (TON) as the molar amount of methanol converted into hydrocarbon products before deactivation normalized to the amount of Brønsted acid sites. The TON values are listed in Table 3. For bulk MFI zeolites, the TON increases in the order [Ga]MFI-bulk > [Al]MFI-bulk > [Fe]MFI-bulk. The [Al]MFI-sheet has the highest TON of all the zeolites, which can be ascribed to the high density of Brønsted acid sites in combination with the open pore architecture, resulting in optimal use of the micropore space and short residence times of precursors to coke. [Ga]MFI-sheet has a much lower TON compared with [Al]MFI-sheet owing to the weaker strength of the acid sites.

## Conclusions

A series of bulk and sheet-like MFI zeolites with varying acidity was obtained by hydrothermal synthesis by using gels containing $Al^{3+}$, $Ga^{3+}$, $Fe^{3+}$, or $B^{3+}$. All obtained materials had the MFI zeolite topology, consisting either of crystals of several hundreds of nanometers (tetrapropylammonium SDA, bulk zeolites) or several-nanometer-thick platelets ($C_{22\text{-}6\text{-}6}$•$Br_2$ SDA, sheet zeolites). NMR spectroscopy showed that a high fraction of the relatively small B and Al cations was inserted in the MFI framework, whereas about half of the Ga and Fe cations ended up in in the framework. The Brønsted acid strength as determined from the bridging hydroxyl frequency shift upon CO adsorption decreased in the order Al(OH)Si > Ga(OH)Si > Fe(OH)Si ≫ B(OH)Si. Judged from the intensity of the band resulting from CO adsorbed on bridging hydroxyl groups, the concentration of Brønsted acid decreased in the order Al(OH)Si > Ga(OH)Si > Fe(OH)Si ≫ B(OH)Si for bulk and Al(OH)Si > Fe(OH)Si > Ga(OH)Si ≫ B(OH)Si for sheet-like zeolites. In particular, the amount of Brønsted acid sites was lower in sheet-like [Ga]MFI in comparison with bulk [Ga]MFI. Pyridine-$^{15}$N NMR spectra showed that there was more than one population of Brønsted acid sites in the zeolites. This was most evident for the [Ga]MFI with one type of acid sites being stronger than the other one. The [B]MFI contained only Brønsted acid sites of the weaker sort. The Lewis acid sites in [B]MFI zeolites were also weaker than those in [Ga]MFI and [Al]MFI zeolites, with the latter samples displaying similar Lewis acid strengths. In general, the acidity in the nanosheet zeolites was weaker than in the bulk zeolites, mainly owing to a lower efficiency in the inclusion of tervalent cations in the framework. The sheet-like Al-based MFI zeolites exhibited the highest longevity in the MTH reaction, strongly outperforming its bulk [Al]MFI counterpart. Although the lower acidity of bulk [Ga]MFI led to better catalytic performance than bulk [Al]MFI, the sheet-like [Ga]MFI sample was found to be nearly inactive. The Fe- and B-substituted zeolite samples displayed very low catalytic performance owing to their too low acidity. Based on the selectivities, the MTH reaction was dominated by olefins-based catalytic cycles. Neverthe-

 

less, the improved catalyst longevity of the sheet-like [Al]MFI zeolite can be attributed to shorter residence time of aromatic coke precursors in the micropores (as evident from the lower ethylene selectivity) than of bulk [Al]MFI zeolite.

## Experimental Section

### Synthesis of the structure directing agent (SDA)

For the synthesis of $[C_{22}H_{45}\text{-}N^{+}(CH_3)_2\text{-}C_6H_{12}\text{-}N^{+}(CH_3)_2\text{-}C_6H_{13}]Br_2$ (denoted as $C_{22\text{-}6\text{-}6}\cdot Br_2$), 1-bromodococane (39 g, 0.1 mol, TCI, 98%) was dissolved in toluene (500 mL, Biosolve, 99.5%) and added dropwise into a mixture of *N*,*N*,*N*′,*N*′-tetramethyl-1,6-diaminohexane (214 mL, 1 mol, Aldrich, 99%) and ethanol (500 mL, Biosolve, 99.8%). The solution was heated at reflux in an oil bath at 413 K for 12 h. After cooling to room temperature, the suspension was cooled at 277 K for 1 h. The white solid was filtered and washed with diethyl ether (Biosolve, 99.5%). The resulting solid product *N*-(6-(dimethylamino)hexyl)-*N*,*N*-dimethyldocosan-1-aminium bromide was dried in a vacuum oven at 323 K overnight. This intermediate product was subsequently reacted with 1-bromohexane (66.0 g, 0.4 mol, Aldrich, 98%) in ethanol (500 mL) at 443 K for 12 h. The resulting solution was cooled at 277 K for 1 h. The white solid in the suspension was filtered, washed with diethyl ether, and dried in a vacuum oven at 323 K overnight.[30]

### Synthesis of zeolites

[T]MFI zeolite nanosheets (T = Al, Ga, Fe or B) were synthesized by using $C_{22\text{-}6\text{-}6}\cdot Br_2$ as the SDA. First, NaOH (Merck, 99%) and $C_{22\text{-}6\text{-}6}\cdot Br_2$ were dissolved in demi-water at 333 K. After cooling to room temperature, a second solution, which was made by mixing aluminium nitrate nonahydrate, gallium nitrate nonahydrate, iron nitrate nonahydrate, or boric acid (Aldrich, reagent grade), tetraethylorthosilicate (TEOS, Merck, 99%), and demi-water, was added under vigorous stirring. The gel compositions employed in the present study are shown in Table 4. After stirring for 1 h, the gel was transferred into a Teflon-lined autoclave, heated to 423 K, and kept at this temperature for 6 days while rotating at 50 rpm.

For the synthesis of bulk [T]MFI (T = Al, Ga, Fe or B) zeolites, tetrapropylammonium hydroxide (TPAOH, Merck, 40%) and TEOS were mixed with demi-water, and added dropwise into a solution obtained by dissolving aluminium nitrate nonahydrate, gallium nitrate nonahydrate, iron nitrate nonahydrate, or boric acid in demi-water. The corresponding gel compositions are also shown in Table 4. After vigorous stirring at room temperature for 1 h, the gel was transferred to a Teflon-lined autoclave and crystallized statically at 443 K for 5 days.

After crystallization, the zeolite products were filtered, washed with copious amounts of demi-water, and dried at 383 K overnight. The zeolites were calcined at 823 K for 10 h under flowing air. To obtain the proton forms of the zeolite, the calcined zeolites were ion-exchanged three times with 1 M $NH_4NO_3$ solutions followed by calcination at 813 K for 4 h under flowing air. The proton form of nanosheet zeolites are denoted as [T]MFI-sheet (T = Al, Ga, Fe, or B), the proton form of bulk zeolites as [T]MFI-bulk (T = Al, Ga, Fe, or B).

**Table 4.** Gel composition of bulk and sheet-like MFI zeolites.

| Zeolite | SDA | Gel composition [molar ratio] | | | | | *T* | *t* |
|---|---|---|---|---|---|---|---|---|
| | | SDA | TEOS | X[a] | NaOH | $H_2O$ | [K] | [days] |
| [Al]MFI-bulk | TPAOH | 30 | 100 | 2 | – | 4500 | 443 | 5 |
| [Ga]MFI-bulk | TPAOH | 30 | 100 | 2 | – | 4500 | 443 | 5 |
| [Fe]MFI-bulk | TPAOH | 30 | 100 | 2 | – | 4500 | 443 | 5 |
| [B]MFI-bulk | TPAOH | 30 | 100 | 2 | – | 4500 | 443 | 5 |
| [Al]MFI-sheet | $C_{22\text{-}6\text{-}6}\cdot Br_2$ | 7.5 | 100 | 2 | 22 | 4000 | 423 | 6 |
| [Ga]MFI-sheet | $C_{22\text{-}6\text{-}6}\cdot Br_2$ | 7.5 | 100 | 2 | 22 | 4000 | 423 | 6 |
| [Fe]MFI-sheet | $C_{22\text{-}6\text{-}6}\cdot Br_2$ | 7.5 | 100 | 2 | 22 | 4000 | 423 | 6 |
| [B]MFI-sheet | $C_{22\text{-}6\text{-}6}\cdot Br_2$ | 7.5 | 100 | 2 | 24[b] | 4000 | 423 | 6 |

[a] Aluminum nitrate nonahydrate ($Al(NO_3)_3\cdot 9H_2O$) for [Al]MFI-bulk and [Al]MFI-sheet; gallium nitrate hydrate ($Ga(NO_3)_3\cdot xH_2O$) for [Ga]MFI-bulk and [Ga]MFI-sheet; iron nitrate nonahydrate ($Fe(NO_3)_3\cdot 9H_2O$) for [Fe]MFI-bulk and [Fe]MFI-sheet; boric acid (BOH) for [B]MFI-bulk and [B]MFI-sheet. [b] More NaOH added into the gel to control the pH so it was same value as the other cases.

### Characterization

The elemental composition of the zeolites was determined by ICP-OES (Spectro CirosCCD ICP optical emission spectrometer). For analysis, an equivolumetric mixture of HF (40 wt% in water), $HNO_3$ (65 wt% in water), and water was used to completely dissolve the zeolites.

XRD patterns were recorded with a Bruker D2 Endeavor powder diffraction system using $CuK_\alpha$ radiation. The scanning speed was $2.4^\circ\,min^{-1}$ in the range 5–40°.

Surface area and porosity of zeolites were determined by Ar physisorption in static mode at 87 K with a Micromeritics ASAP 2020 instrument. The samples were outgassed at 723 K for 4 h prior to the sorption measurements. The BET surface area of the samples was determined from adsorption data in the relative pressure range $p/p_0 = 0.05$–$0.25$. The total pore volume was calculated at $p/p_0 = 0.97$. The micropore volume of sheet-like MFI zeolites was determined by the NLDFT method (Ar at 87 K, assuming slit pores without regularization). The micropore volume of bulk ZSM-5 zeolites was determined by the *t*-plot method by using the Broekhoff–de Boer model with a thickness range of 0.34–0.50 nm. The mesopore volume and mesopore size distribution were determined from the adsorption branch of the isotherms by using the NLDFT method.

**Electron microscopy**: Transmission electron microscopy (TEM) images were taken with a FEI Tecnai 20 at an electron acceleration voltage of 200 kV. Prior to measurement, the catalysts were suspended in ethanol and dispersed over a Cu grid with a holey carbon film. Scanning electron microscopy (SEM) images were taken with a FEI Quanta 200F scanning electron microscope at an accelerating voltage of 3–5 kV.

**Vibrational spectroscopy**: FTIR spectra were recorded in the range 4000–400 $cm^{-1}$ by using a Bruker Vertex V70v instrument. The spectra were acquired at a 2 $cm^{-1}$ resolution and averaged over 64 scans. Typically, an amount of about 10 mg of zeolite was pressed into thin wafers with a diameter of 13 mm and placed inside a controlled-environment infrared transmission cell. Before measurement, the zeolite wafer was first heated to 823 K at a rate of 2 K $min^{-1}$ in artificial air. Then, the cell was outgassed at the final temperature until the residual pressure was below $5\times10^{-5}$ mbar. A background IR spectrum was recorded. For CO adsorption, the sample was cooled to 77 K and CO was introduced into the cell through a sample loop connected to a Valco six-port valve. After each dose, a spectrum was recorded at 77 K. To determine the density of acid sites in the zeolites, pyridine was introduced from an ampoule at its vapor pres-

 

sure at room temperature. The exposure time was 10 min. Afterwards, the cell was evacuated to a pressure lower than $5\times10^{-6}$ mbar and a spectrum was recorded. Further spectra were recorded at 423 K after outgassing for 1 h at 423 K, 573 K, and 773 K. To quantify the amount of Brønsted and Lewis acid sites, molar extinction coefficient values of 0.73 cm μmol$^{-1}$ and 1.11 cm μmol$^{-1}$ were applied, respectively.[48]

**NMR spectroscopy**: Nuclear magnetic resonance (NMR) spectra of the proton form of the MFI zeolites were recorded with a 11.7 T Bruker DMX500 NMR spectrometer operating at 500 MHz for $^{1}$H, 160 MHz for $^{11}$B, 132 MHz for $^{27}$Al, 99 MHz for $^{29}$Si, and 152 MHz for $^{71}$Ga measurements. For the $^{27}$Al, $^{71}$Ga, and $^{11}$B magic angle spinning (MAS) NMR experiments, a standard Bruker MAS probehead was used with a rotor with a diameter of 2.5 mm, operated at a spinning rate of 25 kHz. Quantitative NMR spectra were recorded by using a single excitation pulse of 1 μs and an interscan delay of 1 s. The T atom coordination was estimated by spectral deconvolution and assignment of the respective signal components by comparison with literature data. The $^{27}$Al, $^{71}$Ga, and $^{11}$B chemical shifts were referenced to saturated solutions of $Al(NO_3)_3$, $Ga(NO_3)_3$, and BOH, respectively.

Quantitative $^{29}$Si MAS NMR spectra were recorded at room temperature operating at a sample rotation rate of 10 kHz with rotor diameter of 4 mm, by using a high power proton decoupling direct excitation (DE) pulse sequence with a 54° pulse duration of 3 μs and an interscan delay of 120 s. Tetramethylsilane (TMS) was employed as an external reference.

For cross polarization magic angle spinning (CPMAS) $^{1}$H-$^{15}$N NMR measurements, the sample was first subjected to a dehydration procedure. The sample was placed in special glass tube, which was connected to a vacuum line. After activation at 723 K at a pressure lower than $10^{-5}$ mbar for 6 h, the sample was cooled to room temperature and exposed to pyridine-$^{15}$N (98%, Sigma). After heating at 353 K for 0.5 h, the sample was evacuated at 423 K for 0.5 h to remove physisorbed pyridine. CPMAS $^{1}$H-$^{15}$N NMR spectra were measured at 223 K.

### Catalytic activity measurements

The catalytic performance of the zeolites in methanol-to-hydrocarbons reactions were measured in a quartz tubular fixed-bed reactor with 4 mm inner diameter. Typically, an amount of 50 mg of shaped catalyst (sieve fraction 250–425 μm) was placed in the reactor between two quartz-wool plugs. Prior to the reaction, the catalyst was calcined at 823 K in artificial air for 4 h at a total flow rate of 30 mL min$^{-1}$. The methanol conversion reaction was performed at 673 K. Methanol (Merck, 99%) was introduced to the reactor by flowing He through a saturator kept at 292 K at two weight-hourly space velocities (WHSV) of 2 g g$^{-1}$ h$^{-1}$ and 6 g g$^{-1}$ h$^{-1}$. The effluent was analyzed by an online gas chromatograph (Interscience Compact GC equipped with TCD and FID detectors with RT-Q-Bond and $Al_2O_3$/KCl columns). Dimethyl ether is considered as the reactant. The coke deposited after a reaction time of 24 h was measured by thermogravimetric analysis (TGA) by using a TGA/DSC 1 STAR system from Mettler Toledo. The temperature was increased from room temperature to 1123 K at a rate of 5 K min$^{-1}$ under flowing air (50 mL min$^{-1}$).

## Acknowledgments

*The authors would like to thank the China Scholarship Council for financial support. The authors thank A. M. Elemans-Mehring for ICP-OES analysis and the Soft Matter Cryo-TEM Research Unit of Eindhoven University of Technology for access to TEM facilities. The authors thank Lu Gao for SEM analysis and Arno Hoof-van for TEM analysis.*

## Conflict of interest

*The authors declare no conflict of interest.*

**Keywords:** acidity · methanol-to-hydrocarbons · MFI · morphology · zeolites

[1] a) M. E. Dry, *Catal. Today* **1990**, *6*, 183–206; b) H. Schulz, *Appl. Catal. A* **1999**, *186*, 3–12; c) M. E. Dry, *Catal. Today* **2002**, *71*, 227–241.
[2] a) C. D. Chang, *Catal. Today* **1992**, *13*, 103–111; b) L. Palumbo, F. Bonino, P. Beato, M. Bjørgen, A. Zecchina, S. Bordiga, *J. Phys. Chem. C* **2008**, *112*, 9710–9716; c) D. Mores, E. Stavitski, M. H. F. Kox, J. Kornatowski, U. Olsbye, B. M. Weckhuysen, *Chem. Eur. J.* **2008**, *14*, 11320–11327; d) J. Li, Y. Wei, G. Liu, Y. Qi, P. Tian, B. Li, Y. He, Z. Liu, *Catal. Today* **2011**, *171*, 221–228.
[3] G. T. Kokotailo, S. L. Lawton, D. H. Olson, W. M. Meier, *Nature* **1978**, *272*, 437–438.
[4] a) U. Olsbye, S. Svelle, M. Bjørgen, P. Beato, T. V. W. Janssens, F. Joensen, S. Bordiga, K. P. Lillerud, *Angew. Chem. Int. Ed.* **2012**, *51*, 5810–5831; *Angew. Chem.* **2012**, *124*, 5910–5933; b) K. Hemelsoet, J. Van der Mynsbrugge, K. De Wispelaere, M. Waroquier, V. Van Speybroeck, *ChemPhysChem* **2013**, *14*, 1526–1545.
[5] a) F. J. Keil, *Microporous Mesoporous Mater.* **1999**, *29*, 49–66; b) G. Yang, Y. Wei, S. Xu, J. Chen, J. Li, Z. Liu, J. Yu, R. Xu, *J. Phys. Chem. C* **2013**, *117*, 8214–8222; c) D. Chen, K. Moljord, T. Fuglerud, A. Holmen, *Microporous Mesoporous Mater.* **1999**, *29*, 191–203.
[6] a) W. Dai, G. Wu, L. Li, N. Guan, M. Hunger, *ACS Catal.* **2013**, *3*, 588–596; b) J. F. Haw, D. M. Marcus, *Top. Catal.* **2005**, *34*, 41–48.
[7] J. Li, G. Xiong, Z. Feng, Z. Liu, Q. Xin, C. Li, *Microporous Mesoporous Mater.* **2000**, *39*, 275–280.
[8] L. S. Dent, J. V. Smith, *Nature* **1958**, *181*, 1794–1796.
[9] M. Stöcker, *Microporous Mesoporous Mater.* **1999**, *29*, 3–48.
[10] a) I. M. Dahl, S. Kolboe, *Catal. Lett.* **1993**, *20*, 329–336; b) I. M. Dahl, S. Kolboe, *J. Catal.* **1994**, *149*, 458–464; c) I. M. Dahl, S. Kolboe, *J. Catal.* **1996**, *161*, 304–309.
[11] a) M. Bjørgen, F. Joensen, K. P. Lillerud, U. Olsbye, S. Svelle, *Catal. Today* **2009**, *142*, 90–97; b) M. Bjørgen, S. Svelle, F. Joensen, J. Nerlov, S. Kolboe, F. Bonino, L. Palumbo, S. Bordiga, U. Olsbye, *J. Catal.* **2007**, *249*, 195–207; c) S. Svelle, F. Joensen, J. Nerlov, U. Olsbye, K. P. Lillerud, S. Kolboe, M. Bjørgen, *J. Am. Chem. Soc.* **2006**, *128*, 14770–14771.
[12] Y. V. Kissin, *Catal. Rev. Sci. Eng.* **2001**, *43*, 85–146.
[13] D. Lesthaeghe, A. Horré, M. Waroquier, G. B. Marin, V. Van Speybroeck, *Chem. Eur. J.* **2009**, *15*, 10803–10808.
[14] a) B. Liu, D. Slocombe, M. AlKinany, H. AlMegren, J. Wang, J. Arden, A. Vai, S. Gonzalez-Cortes, T. Xiao, V. Kuznetsov, P. P. Edwards, *Appl. Petrochem. Res.* **2016**, 209–215; b) D. Mores, J. Kornatowski, U. Olsbye, B. M. Weckhuysen, *Chem. Eur. J.* **2011**, *17*, 2874–2884.
[15] W. Song, H. Fu, J. F. Haw, *J. Am. Chem. Soc.* **2001**, *123*, 4749–4754.
[16] a) L. Wu, P. C. M. M. Magusin, V. Degirmenci, M. Li, S. M. T. Almutairi, X. Zhu, B. Mezari, E. J. M. Hensen, *Microporous Mesoporous Mater.* **2014**, *189*, 144–157; b) Y. Yang, C. Sun, J. Du, Y. Yue, W. Hua, C. Zhang, W. Shen, H. Xu, *Catal. Commun.* **2012**, *24*, 44–47; c) M. Bjørgen, F. Joensen, M. Spangsberg Holm, U. Olsbye, K. P. Lillerud, S. Svelle, *Appl. Catal. A* **2008**, *345*, 43–50; d) F. L. Bleken, S. Chavan, U. Olsbye, M. Boltz, F. Ocampo, B. Louis, *Appl. Catal. A* **2012**, *447–448*, 178–185; e) R. Khare, D. Millar, A. Bhan, *J. Catal.* **2015**, *321*, 23–31.
[17] H.-G. Jang, H.-K. Min, S. B. Hong, G. Seo, *J. Catal.* **2013**, *299*, 240–248.

 

[18] A. Mohammadrezaei, S. Papari, M. Asadi, A. Naderifar, R. Golhosseini, *Front. Chem. Sci. Eng.* **2012**, *6*, 253 – 258.
[19] J. Lopez-Sanchez, M. Conte, P. Landon, W. Zhou, J. Bartley, S. Taylor, A. Carley, C. Kiely, K. Khalid, G. Hutchings, *Catal. Lett.* **2012**, *142*, 1049 – 1056.
[20] R. Kawase, A. Iida, Y. Kubota, K. Komura, Y. Sugi, K. Oyama, H. Itoh, *Ind. Eng. Chem. Res.* **2007**, *46*, 1091 – 1098.
[21] I. Yarulina, S. Bailleul, A. Pustovarenko, J. R. Martinez, K. D. Wispelaere, J. Hajek, B. M. Weckhuysen, K. Houben, M. Baldus, V. Van Speybroeck, F. Kapteijn, J. Gascon, *ChemCatChem* **2016**, *8*, 3057 – 3063.
[22] a) E. Lalik, X. Liu, J. Klinowski, *J. Phys. Chem.* **1992**, *96*, 805 – 809; b) L. A. Vostrikova, K. G. Ione, V. M. Mastikhin, A. V. Petrova, *React. Kinet. Catal. Lett.* **1984**, *26*, 291 – 295; c) V. N. Romannikov, L. S. Chumachenko, V. M. Mastikhin, K. G. Ione, *React. Kinet. Catal. Lett.* **1985**, *29*, 85 – 91.
[23] S. Kaliaguine, J. B. Nagy, Z. Gabelica, *Stud. Surf. Sci. Catal.* **1988**, *35*, 381 – 429.
[24] X. Zhu, L. Wu, P. C. M. M. Magusin, B. Mezari, E. J. M. Hensen, *J. Catal.* **2015**, *327*, 10 – 21.
[25] L. Tosheva, V. P. Valtchev, *Chem. Mater.* **2005**, *17*, 2494 – 2513.
[26] a) M. Hartmann, A. G. Machoke, W. Schwieger, *Chem. Soc. Rev.* **2016**, *45*, 3313 – 3330; b) K. Möller, T. Bein, *Chem. Soc. Rev.* **2013**, *42*, 3689 – 3707; c) K. Na, M. Choi, R. Ryoo, *Microporous Mesoporous Mater.* **2013**, *166*, 3 – 19.
[27] a) J. Scherzer, *J. Catal.* **1978**, *54*, 285 – 288; b) C. S. Triantafillidis, A. G. Vlessidis, L. Nalbandian, N. P. Evmiridis, *Microporous Mesoporous Mater.* **2001**, *47*, 369 – 388.
[28] R. M. Dessau, E. W. Valyocsik, N. H. Goeke, *Zeolites* **1992**, *12*, 776 – 779.
[29] a) Z. X. Yang, Y. D. Xia, R. Mokaya, *Adv. Mater.* **2004**, *16*, 727 – 732; b) E. Bekyarova, K. Kaneko, *Adv. Mater.* **2000**, *12*, 1625 – 1628.
[30] M. Choi, K. Na, J. Kim, Y. Sakamoto, O. Terasaki, R. Ryoo, *Nature* **2009**, *461*, 246 – 249.
[31] a) C. T. W. Chu, C. D. Chang, *J. Phys. Chem.* **1985**, *89*, 1569 – 1571; b) P. Strodel, K. M. Neyman, H. Knözinger, N. Rösch, *Chem. Phys. Lett.* **1995**, *240*, 547 – 552; c) H. Berndt, A. Martin, H. Kosslick, B. Lücke, *Microporous Mater.* **1994**, *2*, 197 – 204; d) Y. Ji, B. Shi, H. Yang, W. Yan, *Appl. Catal. A* **2017**, *533*, 90 – 98.
[32] A. J. J. Koekkoek, H. Xin, Q. Yang, C. Li, E. J. M. Hensen, *Microporous Mesoporous Mater.* **2011**, *145*, 172 – 181.
[33] M. Thommes, *Chem. Ing. Tech.* **2010**, *82*, 1059 – 1073.
[34] M. Thommes, K. A. Cychosz, *Adsorption* **2014**, *20*, 233 – 250.
[35] R. de Ruiter, J. C. Jansen, H. van Bekkum, *Zeolites* **1992**, *12*, 56 – 62.
[36] a) G. P. Heitmann, G. Dahlhoff, J. P. M. Niederer, W. F. Hölderich, *J. Catal.* **2000**, *194*, 122 – 129; b) R. Fricke, H. Kosslick, G. N. Lischke, M. Richter, *Chem. Rev.* **2000**, *100*, 2303 – 2406.
[37] a) C. Fild, D. F. Shantz, R. F. Lobo, H. Koller, *Phys. Chem. Chem. Phys.* **2000**, *2*, 3091 – 3098; b) G. L. Turner, K. A. Smith, R. J. Kirkpatrick, E. Oldfield, *J. Magn. Reson.* **1986**, *67*, 544 – 550.
[38] C. T. W. Chu, G. H. Kuehl, R. M. Lago, C. D. Chang, *J. Catal.* **1985**, *93*, 451 – 458.
[39] C. A. Fyfe, Y. Feng, H. Grondey, G. T. Kokotailo, H. Gies, *Chem. Rev.* **1991**, *91*, 1525 – 1543.
[40] H. Kessler, J. M. Chezeau, J. L. Guth, H. Strub, G. Coudurier, *Zeolites* **1987**, *7*, 360 – 366.
[41] S. Ramdas, J. Klinowski, *Nature* **1984**, *308*, 521 – 523.
[42] V. R. Choudhary, A. K. Kinage, C. Sivadinarayana, P. Devadas, S. D. Sansare, M. Guisnet, *J. Catal.* **1996**, *158*, 34 – 50.
[43] V. R. Choudhary, C. Sivadinarayana, A. K. Kinage, *J. Catal.* **1998**, *173*, 243 – 245.
[44] Q. Zhu, B. L. Mojet, R. A. J. Janssen, E. J. M. Hensen, J. van Grondelle, P. C. M. M. Magusin, R. A. van Santen, *Catal. Lett.* **2002**, *81*, 205 – 212.
[45] a) K. Barbera, F. Bonino, S. Bordiga, T. V. W. Janssens, P. Beato, *J. Catal.* **2011**, *280*, 196 – 205; b) H. Knözinger, S. Huber, *J. Chem. Soc. Faraday Trans.* **1998**, *94*, 2047 – 2059; c) M. S. Holm, S. Svelle, F. Joensen, P. Beato, C. H. Christensen, S. Bordiga, M. Bjorgen, *Appl. Catal. A* **2009**, *356*, 23 – 30.
[46] S. M. T. Almutairi, B. Mezari, E. A. Pidko, P. C. M. M. Magusin, E. J. M. Hensen, *J. Catal.* **2013**, *307*, 194 – 203.
[47] a) I. G. Shenderovich, G. Buntkowsky, A. Schreiber, E. Gedat, S. Sharif, J. Albrecht, N. S. Golubev, G. H. Findenegg, H. H. Limbach, *J. Phys. Chem. B* **2003**, *107*, 11924 – 11939; b) G. E. Maciel, J. F. Haw, I. S. Chuang, B. L. Hawkins, T. A. Early, D. R. McKay, L. Petrakis, *J. Am. Chem. Soc.* **1983**, *105*, 5529 – 5535.
[48] J. Datka, A. M. Turek, J. M. Jehng, I. E. Wachs, *J. Catal.* **1992**, *135*, 186 – 199.
[49] a) R. Buzzoni, S. Bordiga, G. Ricchiardi, C. Lamberti, A. Zecchina, G. Bellussi, *Langmuir* **1996**, *12*, 930 – 940; b) C. A. Emeis, *J. Catal.* **1993**, *141*, 347 – 354.
[50] T. R. Hughes, H. M. White, *J. Phys. Chem.* **1967**, *71*, 2192 – 2201.
[51] Z. Liu, X. Dong, Y. Zhu, A. H. Emwas, D. Zhang, Q. Tian, Y. Han, *ACS Catal.* **2015**, *5*, 5837 – 5845.
[52] a) G. J. Hutchings, L. J. van Rensburg, W. Pickl, R. Hunter, *J. Chem. Soc. Faraday Trans.* **1988**, *84*, 1311 – 1328; b) D. Chen, A. Grønvold, K. Moljord, A. Holmen, *Ind. Eng. Chem. Res.* **2007**, *46*, 4116 – 4123.

Manuscript received: June 3, 2017
Accepted manuscript online: June 22, 2017
Version of record online: September 14, 2017

 